Perovskite $Sr_x(Bi_{1-x}Na_{0.97-x}Li_{0.03})_{0.5}TiO_3$ ceramics with polar nano regions for high power energy storage

Jiyue Wu[1], Amit Mahajan[1], Lars Riekehr[2], Hangfeng Zhang[3], Bin Yang[4], Nan Meng[1], Zhen Zhang[2] and Haixue Yan[1*]*

Email: zhen.zhang@angstrom.uu.se, h.x.yan@qmul.ac.uk

[1]*School of Engineering and Materials Science, Queen Mary University of London, Mile End Road, London E1 4NS, UK*

[2]*Division of Solid State Electronics, Department of Engineering Science, Uppsala University, Lagerhyddsvagen, Uppsala, Sweden*

[3]*School of Biological and Chemical Science, Queen Mary University of London, Mile End Road, London E1 4NS, UK*

[4]*Department of Electronic and Electrical Engineering, Faculty of Science and Engineering, University of Chester, Thornton Science Park, CH2 4NU, UK*

Abstract

Dielectric capacitors are very attractive for high power energy storage. However, the low energy density of these capacitors, which is mainly limited by the dielectric materials, is still the bottleneck for their applications. In this work, lead-free single-phase perovskite $Sr_x(Bi_{1-x}Na_{0.97-x}Li_{0.03})_{0.5}TiO_3$ (x=0.30 and 0.38) bulk ceramics, prepared using solid-state reaction method, were carefully studied for the dielectric capacitor application. Polar nano regions (PNRs) were created in this material using co-substitution at A-site to enable relaxor behaviour with low remnant polarization (P_r) and high maximum polarization (P_{max}). Moreover, P_{max} was further increased due to reversible electric field induced phase transitions. Comprehensive structural and electrical studies were performed to confirm the PNRs and the reversible phase transitions. And finally a high energy density (1.70 J/cm^3) with an excellent efficiency (87.2%) was achieved using the contribution of PNRs and field-induced transitions in this material, making it among the best performing lead-free dielectric ceramic bulk material for high energy storage.

Keywords: Relaxor Ferroelectric; Dielectric; Polar Nano Regions; Energy Storage

1. Introduction

Due to the rapid development of electronic devices and power systems, the demand for high power energy storage has been increased significantly in recent years.[1, 2] To address serious concerns on air pollution and climate change, researchers are actively searching for new environmentally friendly energy storage technologies nowadays.[3-7] Compared with chemical batteries[8] and electrochemical capacitors[9], dielectric capacitors have merits of high power density (~GW/kg for ceramic capacitors), short charge/discharge time (~ns) and high cycling reliability (>10^6 cycles).[3, 10] However, the low energy density of dielectric capacitors is the barrier for applications. At present, the typical value of energy density for commercial polymer based capacitors is around 1 J/cm^3 (Biaxially Oriented Polypropylene, BOPP) and even lower for ceramic capacitors (0.1-0.5 J/cm^3).[11] Even though the energy density of ceramic capacitors can be improved by higher applied electrical field, the energy efficiency will be significantly degraded due to higher conductivity and/or irresistible transitions caused by high field.[12, 13] Therefore, a notable improvement in both the energy density and the energy efficiency of ceramic capacitors is critical for their practical applications.[14]

Dielectric oxides thin films usually possess much larger energy density than bulk ceramics since they can withstand higher electric fields before breakdown. However, their practical applications are limited by the substrate effects and difficulties in up-scaling process.[15] In comparison, bulk ceramics capacitors are more compatible with low cost and large scale manufacturing processes. In addition, bulk ceramics offer much larger effective volume and much wider working temperature range for energy storage.[16]

Unlike ferroelectrics with long-range ordered domains and high remnant polarization (P_r), relaxor ferroelectrics (RFEs) possess polar nano regions (PNRs) and normally have negligible P_r, high maximum polarization (P_{max}) and low coercive field (E_c).[17] These properties are vital to achieve high energy density and efficiency in dielectric capacitors for high power energy storage.[18-20] However, RFE systems are relatively limited and the majorities are lead-containing compositions.[21, 22] With serious concern of environmental protection, efforts are being made to develop promising lead-free candidates.[23-25] For instance, microwave-sintered $(Ba_{0.4}Sr_{0.6})TiO_3$ ceramics were reported to exhibit a recoverable energy density of 1.15 J/cm^3 with an efficiency of 82.0%.[26] Xu *et al.* designed a new ternary system ($Bi_{0.5}Na_{0.5}TiO_3$–$BaTiO_3$–$Na_{0.73}Bi_{0.09}NbO_3$), which showed a recoverable energy density of 1.36 J/cm^3 with an efficiency of 73.9%.[27] Despite the significant progress made so far, the demands for lead-free ceramic capacitor materials to achieve high recoverable energy density and optimum energy storage efficiency are still enormous.

In this paper, single-phase lead free perovskite ceramics with the composition of $Sr_x(Bi_{1-x}Na_{0.97-x}Li_{0.03})_{0.5}TiO_3$ (x= 0.30 and 0.38) were designed and synthesized. The design was based on lead-free perovskite-structured $Bi_{0.5}Na_{0.5}TiO_3$ (BNT) with strong ferroelectricity at room temperature and relaxor behaviour at temperatures above 200 °C And since $SrTiO_3$ is an incipient ferroelectric with a cubic perovskite structure at room temperature,[28] Sr^{2+} was introduced in the BNT perovskite structures to break the long-range order of the ferroelectrics to generate PNRs in the matrix, giving the path for relaxor behaviour to be revealed.[29, 30] Li^+ was co-substituted because of its small radius (0.090 nm), which can lead to the distortion of the octahedral [TiO_6] in the lattice to enhance the P_{max} value.[31] Reversible field-induced transitions are responsible for further increasing the energy density.[32] This designed material system indeed shows relaxor behaviour with PNRs and reversible field-induced transitions. A

high energy density with excellent energy efficiency is achieved in the developed bulk ceramics, providing the feasibility for the application in high power energy storage.

2. Experimental

Ceramic powders of $Sr_x(Bi_{1-x}Na_{0.97-x}Li_{0.03})_{0.5}TiO_3$ (x= 0.30 and 0.38) (denoted as SBNLT-30 and SBNLT-38) were prepared via a conventional solid-state reaction process. Powders of Bi_2O_3 (99.9% Sigma-Aldrich), TiO_2 (99.8% Sigma-Aldrich), Na_2CO_3 (99.5% Sigma-Aldrich), $SrCO_3$ (99.5% Alfa Aesar), and Li_2CO_3 (99.0% Alfa Aesar) were used as raw materials. Stoichiometric amounts of powders were weighed according to each formula of composition. The mixture was ball milled for 4 hours in nylon pots using ethanol and zirconia balls. The slurry was then dried in air. Calcination was then carried out at 800 °C for 2 hours followed by 900 °C for 4 hours. The calcined powders were ball milled again for 4 hours in order to obtain homogeneous particle size. After drying, the powders were mixed with binder (5 wt. % polyvinyl alcohol) and then uniaxially cold-pressed into pellets. These pellets were sintered at 1150 °C for 4 hours for densification after binder removed at 600 °C for 2 hours. The pellets were embedded in the calcined powders to avoid the evaporation of Bi and Na elements during sintering.

The density of pellets was measured based on the Archimedes principle. The microstructure of ceramics was examined using an FEI Inspect F (Hillsboro, OR) Scanning Electron Microscope (SEM). The average grain size of ceramics was determined from the fracture surfaces within the range of approximate 400 grains using Image J. The crystallographic structure was characterized using X-ray diffraction (XRD), using a PANalytical X'Pert Pro X-ray diffractometer (PANalytical, Cambridge, UK). It was fitted with an X'Celerator detector in θ/θ geometry using Ni filtered Cu-Kα radiation (λ=1.5418 Å). Data from the X-ray diffractometer

were analysed by the Rietveld method using the FullProf program. The domain structure was characterized using Piezoresponse Force Microscopy (PFM) (NT-MDT, Ntegra systems, Russia), using a conductive tip operated at 50 kHz with a 10 V AC electric field. Before the PFM imaging, the sample was polished then thermal-etched at 1050 °C for 15 minutes. The domain structure was visualized through monitoring the first harmonics of the deflection signal. The bulk ceramic sample for Transmission Electron Microscopy (TEM) analysis was prepared by mechanical polishing, dimpling and ion milling until electron transparency was reached in the centre of a 3 mm disc. The TEM investigation was carried out on a FEI Titan Themis operating at an acceleration voltage of 200 kV.

Silver paste (Gwent Electronic Materials Ltd., C2011004D5, Pontypool, U.K.) was homogenously covered at the top and bottom of discs with an average thickness of around 0.3 mm, and then fired at 600 °C for 30 minutes to obtain smooth electrodes for electric characterization. The temperature dependence of dielectric constant (ε_r) and loss (tan δ) was measured at six different frequencies in the range of 100 Hz to 100 kHz, using an LCR meter (Agilent, 4284A, Hyogo, Japan) with controlled temperature from -160 °C to 160 °C. Current-polarization-electric field (*I-P-E*) hysteresis loops were measured using a hysteresis tester (NPL, Teddington, U.K.) and triangle waveforms at room temperature and 10 Hz.[33]

3. Results and Discussion

3.1 Phase and Composition

The relative density of SBNLT-30 and SBNLT-38 is 96%. Room-temperature XRD patterns and Rietveld refinement data are shown in Figure 1. The two samples show identical diffraction reflections, indicating the homogenous perovskite structure and no secondary phase can be detected. With the magnification in the 2θ range of 38^o-48^o (Figure 1(c) and (d)), the (111) and

(200) reflections are accurately fitted by the cubic (*Pm*3*m*) model. Thus, no evidence of rhombohedral or tetragonal distortion can be detected. Fitting parameters are summarized in Table 1. The fitting is proved to be reliable with the cubic model, since the fitting goodness χ^2 and R_{wp} show low values. The volume of unit cell of SBNLT-38 is larger than that of SNBLT-30 (Table 1), which demonstrates the fact that Sr^{2+} ions were introduced into the lattice.

Figure 2 shows the SEM images of SBNLT ceramics. The samples of SBNLT-30 and SBNLT-38 exhibit homogenous and dense microstructure with an average grain size of 2.4 μm and 2.9 μm, respectively.

3.2 Dielectric Properties

Figure 3 shows the temperature dependence of dielectric permittivity (ε_r) and loss tangent (tanδ) for both compositions. Only one peak corresponding to the maximum ε_r can be observed for both samples, the temperature of which is assigned as T_m. Moreover, with increasing frequency, ε_r decreases and T_m shifts to a higher temperature, which is a typical characteristic of RFE. The peak of SBNLT-38 is more flat compared to SBNLT-30, suggesting the positive contribution of Sr^{2+} in revealing relaxor behaviour. A higher amount of Sr^{2+} favours the disruption of long-range ferroelectric order of BNT, which is also supported by a lower T_m (closer to room temperature) of SBNLT-38.

Taking a further look into the relaxor behaviour, the freezing temperature T_{VF} is the 'static' dipolar freezing temperature for relaxation described by Vogel-Fulcher relation:[34, 35]

$$\tau = \tau_0 exp\left[\frac{E_a}{k_B(T_m - T_{VF})}\right]$$

where τ is the relaxation time in relaxors, τ_0 is the pre-exponential factor, E_a is the activation energy for the fluctuation of each isolated PNR, k_B is the Boltzmann constant, T_m is the temperature corresponding to the dielectric maxima and T_{VF} is the 'static' dipolar freezing temperature for relaxation. The temperature-dependent relaxation time of both compositions can be properly fitted by Vogel-Fulcher relation (Figure 4 and Table 2). For SBNLT-30 and SBNLT-38, both the fitting values of T_{VF} are below room temperature. Consequently, at room temperature (above T_{VF}), PNRs can be reversibly transformed into strong polar structures with applied electric field, which may generate slim hysteresis ferroelectric loops,[36] and more details will be discussed later in the ferroelectric characterization part.

3.3 Microstructure discussion

PFM was used to demonstrate the existence of polar structure in nanoscale. The contrast of signal with phase depends on both the amplitude of piezoelectric coefficient (d_{33}) and polarization deflection. The bright areas on the phase image illustrate polarization directed towards the bottom electrode while dark areas correspond to the domains of opposite direction.[37] In this case, vertical PFM scanning was performed on the sample of SBNLT-30 with a chosen area of 5×5 μm^2. The topography and magnitude are shown in Figure 5(a) and 5(b), respectively. In Figure 5(c1), there is no evident domain structure according to the phase response. This case is different from other reported BNT systems, which have macroscopic domains.[38, 39] Figure 5(c2) shows the height and phase signal collected from the original surface. Different tendencies between phase and height illustrate the piezo-response, being consistent with the contrast observed in Figure 5(c1).

A DC bias voltage of 30 V was applied in the centre of the area (3×3 μm^2) for 5 minutes to observe structural change. Comparing the signal with phase (Figure 5(c1, d1 and e1)) along

with the variation (Figure 5(c2, d2 and e2)), the difference in contrast can be revealed. The dark regions after poling denote the change of polarization of samples, indicating the ferroelectric behaviour. However, no clear patterns of ferroelectric domains can be observed, which is probably due to the fact that PNRs are too tiny (a few nanometres) for the resolution of PFM. This interpretation is consistent with the XRD results (Figure 1), indicating no structural distortion. Meanwhile, the contrast of the area faded with time passing, which shows the relaxor behaviour of PNRs (Figure 5(f1) and (f2)).

To further verify the existence of polar structure in nanoscale, a representative grain of SBNLT-30 was analyzed using TEM. Oxygen octahedral distortions cause reflections which can be used to discriminate the cubic, tetragonal and rhombohedral phase. The intensity is extremely hard to be detected in XRD analysis, but can be identified using Selected Area Electron Diffraction (SAED).[40] In Figure 6(a), a SAED pattern along [110] zone axis is depicted. The pattern is indexed with cubic *Pm*3*m* symmetry but additional super-lattice reflections are detected along the [110] zone axis, only *1/2 (ooo)* spots (marked by bright arrows) are detected without *1/2 (ooe)* reflections (*o* stands for odd and *e* stands for even Miller indices). This finding proves the *R*3*c* distortion and refutes the existences of the tetragonal distortion.[41, 42] The contrast in dark field (DF) image (Figure 6(b)) gives direct evidence that PNRs are homogeneously distributed in the selected grain, supporting the macroscopic relaxor behaviour observed in dielectric spectroscopy (Figure 3). From the TEM study on SBNLT-30, polar structure (*R*3*c*) exists in the form of PNRs in nanoscale.

3.4 Ferroelectric & Energy Storage Properties

Figure 7 shows the current-electric field (*I*-*E*) and polarization-electric field (*P*-*E*) loops of both compositions. SBNLT-30 and SBNLT-38 exhibit typical relaxor behaviour, showing high P_{max}

values (33.89 μC/cm^2 and 26.75 μC/cm^2, respectively) and low P_r values (0.87 μC/cm^2 and 1.09 μC/cm^2, respectively), which are both favourable for energy storage (Figure 7(a) and (b)). The dominant position of long-range order ferroelectric structure in BNT is destroyed by the introduction of Sr^{2+}, as evidenced by the evolution of *P*-*E* loops. Similar results were reported in BNT-BT-$K_{0.5}Na_{0.5}NbO_3$ (KNN), where KNN breaks the long-range ferroelectric order of BNT-BT.[43] Moreover, our SBNLT samples, especially SBNLT-30, show four current peaks in the *I*-*E* loops (Figure 7(c) and (d)). In order to understand the details of the loops in Figure 7 for energy storage properties, four standard dielectrics including linear dielectrics (LD), ferroelectrics (FE), relaxor ferroelectrics (RFE) and antiferroelectrics/antiferroelectrics-like (AFE/AFE-like) are illustrated in Figure 8. Their recoverable energy density (W_{rec}) can be calculated by the integral $W_{rec} = \int_{P_r}^{P_{max}} EdP$ (marked in Figure 8), where *E* is the applied field, *P* is the polarization, P_{max} and P_r are the maximum polarization and remnant polarization, respectively. The energy loss density (W_{loss}) is demonstrated by the enclosed area of hysteresis loops in the first quart, and $W_{rec}/(W_{rec} + W_{loss})$ represents the energy efficiency (η).[44] The polarization mechanism of the four materials is illustrated in Figure 8 as well. In Figure 8(a), LDs (e.g., Al_2O_3) show a field-independent current value in the corresponding *I*-*E* loop, which is due to the stable permittivity contributed only from electronic and atomic polarization. Thus, they are restricted in high energy storage applications (low W_{rec}) although they usually possess a low W_{loss} due to negligible P_r. For FEs (e.g., $PbTiO_3$) (Figure 8(b)), the existence of ferroelectric domains makes them promising to achieve high polarization. The two current peaks in the first and third quadrants in the *I*-*E* loop can be attributed to the ferroelectric domain switching. FEs suffer from a high W_{loss} due to the domain switching, leading to a low η. For RFEs (e.g., $Pb(Mg_{1/3}Nb_{2/3})O_3$) (Figure 8(c)), they lack the long-range ferroelectric order with only local polarization occurring in PNRs. Most of the PNRs can be oriented along the direction of the electric field (some PNRs can grow and more PNRs may appear) during loading and

return to their random orientations during unloading (above T_f).[45] This is linked with the two current peaks near zero electric field in the *I-E* loop. RFEs usually possess high P_{max} with low P_r and E_c, but their breakdown fields are normally low, restraining them from achieving a high W_{rec}. For AFEs (e.g., (Pb, La)(Zr, Ti)O_3) (Figure 8(d)), the polarization directions of adjacent dipoles are anti-parallel, but they can be re-arrayed with sufficient electric field during charging. The large W_{rec} results from reversible field-induced antiferroelectric-to-ferroelectric (AFE-FE) phase transitions.[46] They are related to the four current peaks in the four quadrants in the *I-E* loop. As is shown in Figure 8(d), the AFE-FE phase transition takes place when the electric field reaches a critical value (forward field, E_f). As the electric field decreases to lower critical value (backward field, E_b), the FE phase transfer back to AFE phase. When E_f shifts to a lower value, the difference between E_f and E_b (ΔE) becomes smaller, introducing a smaller loops a higher η by reducing W_{loss}. In another way, ΔE becomes smaller when E_b shifts to a higher value, contributing to a higher η value by improving W_{rec} at the same time.

As is shown in Figure 7(c) and (d), the four current peaks in the *I-E* loops are AFE-like (BNT-based materials were reported as AFE, but recent literature prefer AFE-like due to) and different from classic relaxors which only show two current peaks as illustrated in Figure 8(c)). The phenomenon in Figure 7(c) and (d) can be attributed to the reversible field-induced phase transitions: the weak-polar or non-polar phase is transferred to strong-polar phase corresponding to the first current peak (P_1 and P'_1) when loading, and it turns back to the original state upon unloading corresponding to the second current peak (P_2 and P'_2).[32, 47] This interpretation is supported by the TEM investigation in BNT-6%BT ceramics, showing the electrical field-induced transitions from weak-polar (*P*4*nm*) to strong-polar (*R*3*c* + *P*4*mm*) ferroelectric phase symmetry.[48]

In our materials, the values of W_{rec} are 1.70 J/cm^3 and 1.10 J/cm^3 at their maximum electric fields (blue hatched area in Figure 7(a) and (b)), and the corresponding η values are 87.2% and 81.9% for SBNLT-30 and SBNLT-38, respectively. The excellent energy storage properties originate from the RFE behaviour along with the field-induced transitions. Distinguished from classic RFE materials, the reversible field-induced transitions contribute to an additional increase in P_{max}, and further enhance the energy density of our SBNLT ceramics with PNRs. Meanwhile, the slim shape of hysteresis loops (Figure 7(c) and (d)) leads to an ultrahigh η, evidenced by the low values of ΔE (between P_1 and P_2 in Figure 7), which can be attributed to the contribution of PNRs, it is diffent with standard AFE including Domains in FE pahse. In practical applications, η is extremely important because higher η ensures less energy dissipation during charging and discharging, which can deteriorate electric properties and shorten the lifetime.[49] Figure 9 benchmarks the energy storage performance for lead-free ceramic systems reported so far. Note that our SBNLT-30 possesses a high W_{rec} with a superior η, making it very attractive in advanced pulse power system.

4. Conclusion

Single-phase perovskite SBNLT ceramics were designed and successfully prepared via the conventional solid-state reaction method. The temperature dependence of permittivity and loss at different frequencies shows typical relaxor behaviour. The nano-structures were further investigated using PFM and TEM, which elucidates the contribution of PNRs. The evolution of *P-E* loops demonstrates that Sr^{2+} disrupts the long-range ferroelectric order in the BNT system, which induced markedly-reduced P_r value with the increased P_{max} value related to reversible field-induced transitions. The recoverable energy density for SBNLT-30 can be achieved up to 1.70 J/cm^3 at 130 kV/cm, with an ultrahigh energy efficiency of 87.2%. This

work demonstrates that the SBNLT ceramics can be considered as a competitive material for high power energy storage with excellent efficiency.

Acknowledgements

Authors thanks for financial support from EPSRC (MASSIVE project EP/L017695/1; Teranet fund EP/M00306X/1), China Scholarship Council (CSC), the Swedish Strategic Research Foundation (FFL15-0174) and the Wallenberg Academy Fellow Program (Sweden).

References

[1] J. Bae, M.K. Song, Y.J. Park, J.M. Kim, M. Liu, Z.L. Wang, Fiber Supercapacitors Made of Nanowire- Fiber Hybrid Structures for Wearable/Flexible Energy Storage, Angewandte Chemie International Edition 50(7) (2011) 1683-1687.

[2] J. Bae, Y.J. Park, M. Lee, S.N. Cha, Y.J. Choi, C.S. Lee, J.M. Kim, Z.L. Wang, Single-Fiber- Based Hybridization of Energy Converters and Storage Units Using Graphene as Electrodes, Advanced Materials 23(30) (2011) 3446-3449.

[3] Q. Li, L. Chen, M.R. Gadinski, S. Zhang, G. Zhang, H.U. Li, E. Iagodkine, A. Haque, L.-Q. Chen, T.N. Jackson, Q. Wang, Flexible high-temperature dielectric materials from polymer nanocomposites, Nature 523 (2015) 576.

[4] S.L. Candelaria, Y. Shao, W. Zhou, X. Li, J. Xiao, J.-G. Zhang, Y. Wang, J. Liu, J. Li, G. Cao, Nanostructured carbon for energy storage and conversion, Nano Energy 1(2) (2012) 195-220.

[5] C. Liu, F. Li, L.P. Ma, H.M. Cheng, Advanced Materials for Energy Storage, Advanced Materials 22(8) (2010) E28-E62.

[6] B. Dunn, H. Kamath, J.-M. Tarascon, Electrical Energy Storage for the Grid: A Battery of Choices, Science 334(6058) (2011) 928-935.

[7] Z.-S. Wu, G. Zhou, L.-C. Yin, W. Ren, F. Li, H.-M. Cheng, Graphene/metal oxide composite electrode materials for energy storage, Nano Energy 1(1) (2012) 107-131.

[8] J.H. Pikul, H. Gang Zhang, J. Cho, P.V. Braun, W.P. King, High-power lithium ion microbatteries from interdigitated three-dimensional bicontinuous nanoporous electrodes, Nature Communications 4 (2013) 1732.

[9] Z.S. Wu, K. Parvez, X. Feng, K. Müllen, Graphene-based in-plane micro-supercapacitors with high power and energy densities, Nature Communications 4 (2013) 2487.

[10] Q. Li, K. Han, M.R. Gadinski, G. Zhang, Q. Wang, High Energy and Power Density Capacitors from Solution- Processed Ternary Ferroelectric Polymer Nanocomposites, Advanced Materials 26(36) (2014) 6244-6249.

[11] N. Meng, X. Zhu, R. Mao, M.J. Reece, E. Bilotti, Nanoscale interfacial electroactivity in PVDF/PVDF-TrFE blended films with enhanced dielectric and ferroelectric properties, Journal of Materials Chemistry C 5(13) (2017) 3296-3305.

[12] X. Hao, A review on the dielectric materials for high energy-storage application, Journal of Advanced Dielectrics 03(01) (2013) 1330001.

[13] F. Yan, H. Yang, Y. Lin, T. Wang, Dielectric and Ferroelectric Properties of $SrTiO_3$–$Bi_{0.5}Na_{0.5}TiO_3$–$BaAl_{0.5}Nb_{0.5}O_3$ Lead-Free Ceramics for High-Energy-Storage Applications, Inorganic Chemistry 56(21) (2017) 13510-13516.

[14] H. Chen, T.N. Cong, W. Yang, C. Tan, Y. Li, Y. Ding, Progress in electrical energy storage system: A critical review, Progress in Natural Science 19(3) (2009) 291-312.

[15] X. Wei, H. Yan, T. Wang, Q. Hu, G. Viola, S. Grasso, Q. Jiang, L. Jin, Z. Xu, M.J. Reece, Reverse boundary layer capacitor model in glass/ceramic composites for energy storage applications, Journal of Applied Physics 113(2) (2013) 024103.

[16] Y. Tian, L. Jin, H. Zhang, Z. Xu, X. Wei, E.D. Politova, S.Y. Stefanovich, N.V. Tarakina, I. Abrahams, H. Yan, High energy density in silver niobate ceramics, Journal of Materials Chemistry A 4(44) (2016) 17279-17287.

[17] S. Annie, R. Jean, M. Mario, The crossover from a ferroelectric to a relaxor state in lead-free solid solutions, Journal of Physics: Condensed Matter 16(6) (2004) 963.

[18] L.E. Cross, Relaxor ferroelectrics, Ferroelectrics 76(1) (1987) 241-267.

[19] V.V. Shvartsman, D.C. Lupascu, D.J. Green, Lead- Free Relaxor Ferroelectrics, Journal of the American Ceramic Society 95(1) (2012) 1-26.

[20] N. Ortega, A. Kumar, J.F. Scott, B.C. Douglas, M. Tomazawa, K. Shalini, D.G.B. Diestra, R.S. Katiyar, Relaxor-ferroelectric superlattices: high energy density capacitors, Journal of Physics: Condensed Matter 24(44) (2012) 445901.

[21] G. Burns, F.H. Dacol, Glassy polarization behavior in ferroelectric compounds $Pb(Mg_{1/3}Nb_{2/3})O_3$ and $Pb(Zn_{1/3}Nb_{2/3})O_3$, Solid State Communications 48(10) (1983) 853-856.

[22] S.M. Gupta, D. Viehland, Role of charge compensation mechanism in La- modified $Pb(Mg_{1/3}Nb_{2/3})O_3$–$PbTiO_3$ ceramics: Enhanced ordering and pyrochlore formation, Journal of Applied Physics 80(10) (1996) 5875-5883.

[23] F. Gao, X. Dong, C. Mao, W. Liu, H. Zhang, L. Yang, F. Cao, G. Wang, J. Jones, Energy-Storage Properties of $0.89Bi_{0.5}Na_{0.5}TiO_3$–$0.06BaTiO_3$–$0.05K_{0.5}Na_{0.5}NbO_3$ Lead- Free Anti-ferroelectric Ceramics, Journal of the American Ceramic Society 94(12) (2011) 4382-4386.

[24] Q. Xu, M.T. Lanagan, X. Huang, J. Xie, L. Zhang, H. Hao, H. Liu, Dielectric behavior and impedance spectroscopy in lead-free BNT–BT–NBN perovskite ceramics for energy storage, Ceramics International 42(8) (2016) 9728-9736.

[25] L. Luo, B. Wang, X. Jiang, W. Li, Energy storage properties of $(1-x)(Bi_{0.5}Na_{0.5})TiO_3$–$xKNbO_3$ lead-free ceramics, Journal of Materials Science 49(4) (2014) 1659-1665.

[26] Z. Song, S. Zhang, H. Liu, H. Hao, M. Cao, Q. Li, Q. Wang, Z. Yao, Z. Wang, M.T. Lanagan, J. Jones, Improved Energy Storage Properties Accompanied by Enhanced Interface Polarization in Annealed Microwave- Sintered BST, Journal of the American Ceramic Society 98(10) (2015) 3212-3222.

[27] Q. Xu, H. Liu, Z. Song, X. Huang, A. Ullah, L. Zhang, J. Xie, H. Hao, M. Cao, Z. Yao, A new energy-storage ceramic system based on $Bi_{0.5}Na_{0.5}TiO_3$ ternary solid solution, Journal of Materials Science: Materials in Electronics 27(1) (2016) 322-329.

[28] J.H. Haeni, P. Irvin, W. Chang, R. Uecker, P. Reiche, Y.L. Li, S. Choudhury, W. Tian, M.E. Hawley, B. Craigo, A.K. Tagantsev, X.Q. Pan, S.K. Streiffer, L.Q. Chen, S.W. Kirchoefer, J. Levy, D.G. Schlom, Room-temperature ferroelectricity in strained $SrTiO_3$, Nature 430 (2004) 758.

[29] Y. Hiruma, Y. Imai, Y. Watanabe, H. Nagata, T. Takenaka, Large electrostrain near the phase transition temperature of $(Bi_{0.5}Na_{0.5})TiO_3$–$SrTiO_3$ ferroelectric ceramics, Applied Physics Letters 92(26) (2008) 262904.

[30] W. Krauss, D. Schütz, F.A. Mautner, A. Feteira, K. Reichmann, Piezoelectric properties and phase transition temperatures of the solid solution of $(1-x)(Bi_{0.5}Na_{0.5})TiO_3$–$xSrTiO_3$, Journal of the European Ceramic Society 30(8) (2010) 1827-1832.

[31] D. Lin, D. Xiao, J. Zhu, P. Yu, Piezoelectric and ferroelectric properties of $[Bi_{0.5}(Na_{1-x-y}K_xLi_y)_{0.5}]TiO_3$ lead-free piezoelectric ceramics, Applied Physics Letters 88(6) (2006) 062901.

[32] G. Viola, R. McKinnon, V. Koval, A. Adomkevicius, S. Dunn, H. Yan, Lithium-Induced Phase Transitions in Lead-Free $Bi_{0.5}Na_{0.5}TiO_3$ Based Ceramics, The Journal of Physical Chemistry C 118(16) (2014) 8564-8570.

[33] H. Yan, F. Inam, G. Viola, H. Ning, H. Zhang, Q. Jiang, T. Zeng, Z. Gao, M.J. Reece, The contribution of electrical conductivity, dielectric permittivity and domain switching in ferroelectric hysteresis loops Journal of Advanced Dielectrics 01(01) (2011) 107-118.

[34] H. Vogel, The law of the relation between the viscosity of liquids and the temperature, Phys. Z 22 (1921) 645-646.

[35] G.S. Fulcher, Analysis of recent measurements of the viscosity of glasses, Journal of the American Ceramic Society 8(6) (1925) 339-355.

[36] Y. Xi, C. Zhili, L.E. Cross, Polarization and depolarization behavior of hot pressed lead lanthanum zirconate titanate ceramics, Journal of Applied Physics 54(6) (1983) 3399-3403.

[37] A.L. Kholkin, I.K. Bdikin, D.A. Kiselev, V.V. Shvartsman, S.-H. Kim, Nanoscale characterization of polycrystalline ferroelectric materials for piezoelectric applications, Journal of Electroceramics 19(1) (2007) 83-96.

[38] R. Dittmer, W. Jo, J. Rödel, S. Kalinin, N. Balke, Nanoscale Insight Into Lead- Free BNT- BT- xKNN, Advanced Functional Materials 22(20) (2012) 4208-4215.

[39] V.V. Shvartsman, B. Dkhil, A.L. Kholkin, Mesoscale Domains and Nature of the Relaxor State by Piezoresponse Force Microscopy, Annual Review of Materials Research 43(1) (2013) 423-449.

[40] C.A. Randall, D.J. Barber, R.W. Whatmore, P. Groves, A TEM study of ordering in the perovskite, $Pb(Sc_{1/2}Ta_{1/2})O_3$, Journal of Materials Science 21(12) (1986) 4456-4462.

[41] C. Ma, X. Tan, E. Dul'kin, M. Roth, Domain structure-dielectric property relationship in lead-free $(1-x)(Bi_{1/2}Na_{1/2})TiO_3$-$xBaTiO_3$ ceramics, Journal of Applied Physics 108(10) (2010) 104105.

[42] I. Levin, I.M. Reaney, Nano- and Mesoscale Structure of $Na_{1\backslash 2}Bi_{1\backslash 2}TiO_3$: A TEM Perspective, Advanced Functional Materials 22(16) (2012) 3445-3452.

[43] S.-T. Zhang, A.B. Kounga, E. Aulbach, H. Ehrenberg, J. Rödel, Giant strain in lead-free piezoceramics $Bi_{0.5}Na_{0.5}TiO_3$–$BaTiO_3$–$K_{0.5}Na_{0.5}NbO_3$ system, Applied Physics Letters 91(11) (2007) 112906.

[44] Z.M. Dang, J.K. Yuan, S.H. Yao, R.J. Liao, Flexible Nanodielectric Materials with High Permittivity for Power Energy Storage, Advanced Materials 25(44) (2013) 6334-6365.

[45] G.A. Samara, Ferroelectricity revisited—Advances in materials and physics, in: H. Ehrenreich, F. Spaepen (Eds.), Solid State Physics, Academic Press2001, pp. 239-458.

[46] P. Wawrzała, J. Korzekwa, Charge-Discharge Properties of PLZT x/90/10 Ceramics, Ferroelectrics 446(1) (2013) 91-101.

[47] A. Mahajan, H. Zhang, J. Wu, E.V. Ramana, M.J. Reece, H. Yan, Effect of Phase Transitions on Thermal Depoling in Lead-Free $0.94(Bi_{0.5}Na_{0.5}TiO_3)$–$0.06(BaTiO_3)$ Based Piezoelectrics, The Journal of Physical Chemistry C 121(10) (2017) 5709-5718.

[48] C. Ma, H. Guo, S.P. Beckman, X. Tan, Creation and Destruction of Morphotropic Phase Boundaries through Electrical Poling: A Case Study of Lead-Free $Bi_{1/2}Na_{1/2}TiO_3$-$BaTiO_3$ Piezoelectrics, Physical Review Letters 109(10) (2012) 107602.

[49] H. Wang, J. Liu, J. Zhai, B. Shen, M. Cain, Ultra High Energy- Storage Density in the Barium Potassium Niobate- Based Glass- Ceramics for Energy- Storage Applications, Journal of the American Ceramic Society 99(9) (2016) 2909-2912.

[50] Z. Yang, H. Du, S. Qu, Y. Hou, H. Ma, J. Wang, J. Wang, X. Wei, Z. Xu, Significantly enhanced recoverable energy storage density in potassium-sodium niobate-based lead free ceramics, Journal of Materials Chemistry A 4(36) (2016) 13778-13785.

[51] D. Zheng, R. Zuo, D. Zhang, Y. Li, X. Tan, Novel $BiFeO_3$–$BaTiO_3$–$Ba(Mg_{1/3}Nb_{2/3})O_3$ Lead- Free Relaxor Ferroelectric Ceramics for Energy- Storage Capacitors, Journal of the American Ceramic Society 98(9) (2015) 2692-2695.

[52] T. Wang, L. Jin, C. Li, Q. Hu, X. Wei, D. Lupascu, Relaxor Ferroelectric $BaTiO_3$–$Bi(Mg_{2/3}Nb_{1/3})O_3$ Ceramics for Energy Storage Application, Journal of the American Ceramic Society 98(2) (2015) 559-566.

[53] L. Zhao, J. Gao, Q. Liu, S. Zhang, J.-F. Li, Silver Niobate Lead-Free Antiferroelectric Ceramics: Enhancing Energy Storage Density by B-Site Doping, ACS Applied Materials & Interfaces 10(1) (2018) 819-826.

[54] T. Wang, L. Jin, Y. Tian, L. Shu, Q. Hu, X. Wei, Microstructure and ferroelectric properties of Nb_2O_5-modified $BiFeO_3$-$BaTiO_3$ lead-free ceramics for energy storage, Materials Letters 137 (2014) 79-81.

[55] Q. Xu, T. Li, H. Hao, S. Zhang, Z. Wang, M. Cao, Z. Yao, H. Liu, Enhanced energy storage properties of $NaNbO_3$ modified $Bi_{0.5}Na_{0.5}TiO_3$ based ceramics, Journal of the European Ceramic Society 35(2) (2015) 545-553.

[56] J. Hao, Z. Xu, R. Chu, W. Li, D. Juan, F. Peng, Enhanced energy-storage properties of $(1-x)[(1-y)(Bi_{0.5}Na_{0.5})TiO_3–y(Bi_{0.5}K_{0.5})TiO_3]–x(K_{0.5}Na_{0.5})NbO_3$ lead-free ceramics, Solid State Communications 204 (2015) 19-22.

[57] W. Cao, W. Li, Y. Feng, T. Bai, Y. Qiao, Y. Hou, T. Zhang, Y. Yu, W. Fei, Defect dipole induced large recoverable strain and high energy-storage density in lead-free $Na_{0.5}Bi_{0.5}TiO_3$-based systems, Applied Physics Letters 108(20) (2016) 202902.

Table 1. Structural parameters of Rietveld refinement of cubic phase (*Pm*3*m*) for SBNLT-30 and SBNLT-38

Compositions of samples	**Structures and parameters of unit cell (Å)**	**Fitting parameters**
SBNLT-30	**Cubic (*Pm*3*m*) phase**	$\chi^2 = 2.219$
	a = b = c = 3.9019 (Å)	$R_{wp} = 0.0989$
	$\alpha = \beta = \gamma = 90^\circ$	$R_p = 0.0784$
	Volume = 59.408 ($Å^3$)	
SBNLT-38	**Cubic (*Pm*3*m*) phase**	$\chi^2 = 2.238$
	a = b = c = 3.9039 (Å)	$R_{wp} = 0.0989$
	$\alpha = \beta = \gamma = 90^\circ$	$R_p = 0.0770$
	Volume = 59.499 ($Å^3$)	

Table 2. Summary of the Vogel-Fulcher fitting parameters of SBNLT-30 and SBNLT-38

Sample	**Freezing temperature T_{VF} / K**	**Activation energy E_a / eV**	**Pre-exponential factor τ_0 / s**
SBNLT-30	290 (±5)	0.025 (±0.01)	3.06×10^{-13}

SBNLT-38	179 (±8)	0.058 (±0.01)	1.48×10^{-12}

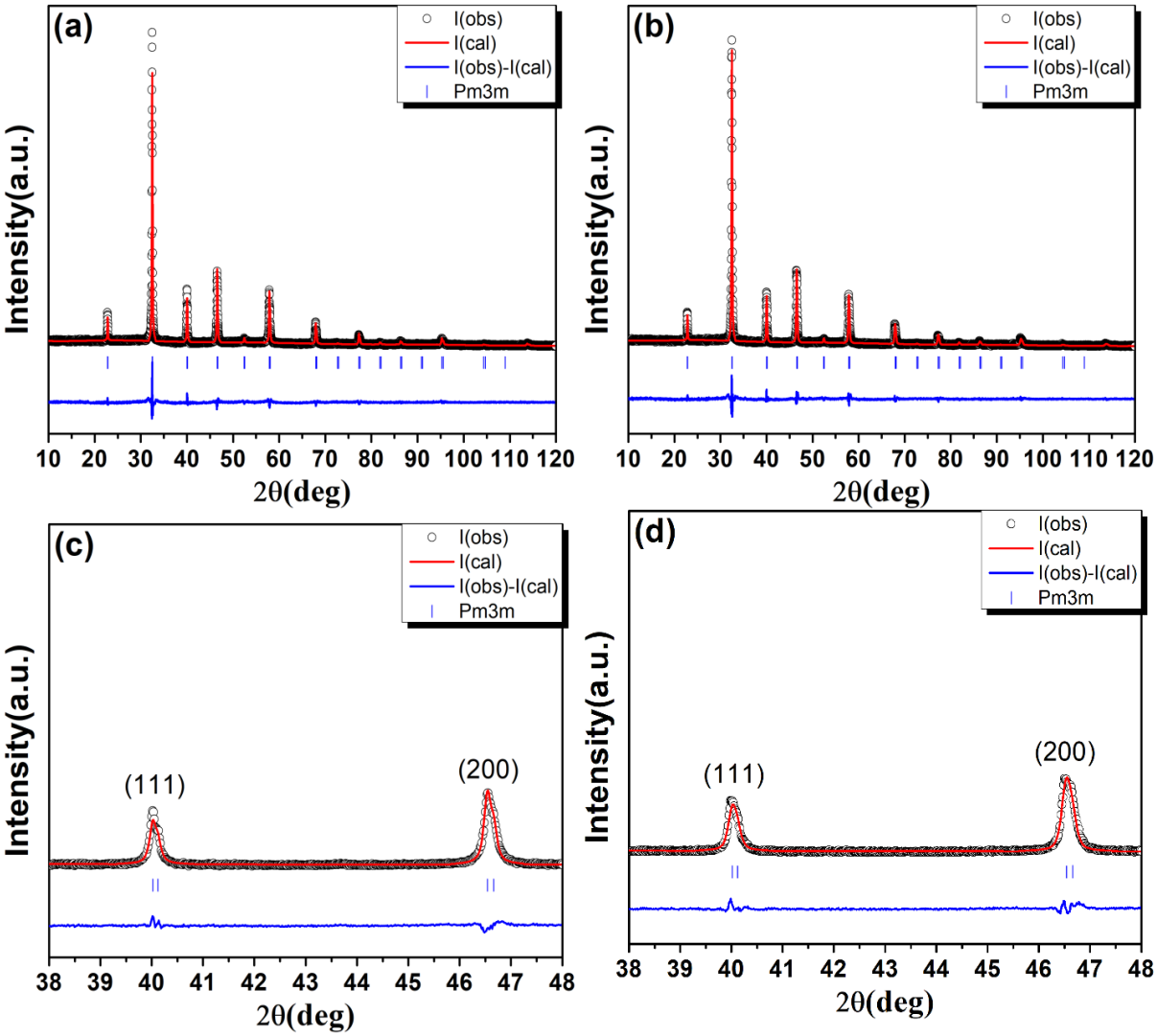

Figure 1. Rietveld fitted XRD patterns of SBNLT-x: (a) x = 30 and (b) x = 38, both fitted with *Pm*3*m* structure model. Locally magnified (111) and (200) diffraction peak for SBNLT-x: (c) x = 30 and (d) x = 38.

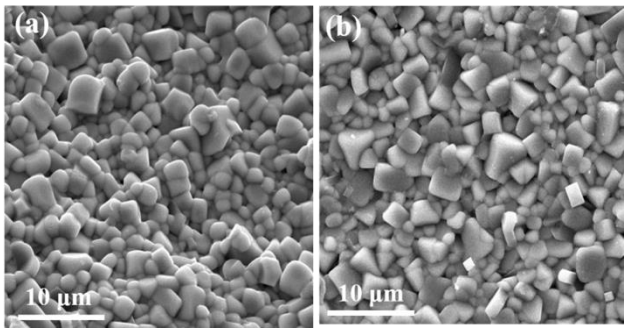

Figure 2. SEM images of fracture surfaces of SBNLT-x: (a) x = 30 and (b) x = 38.

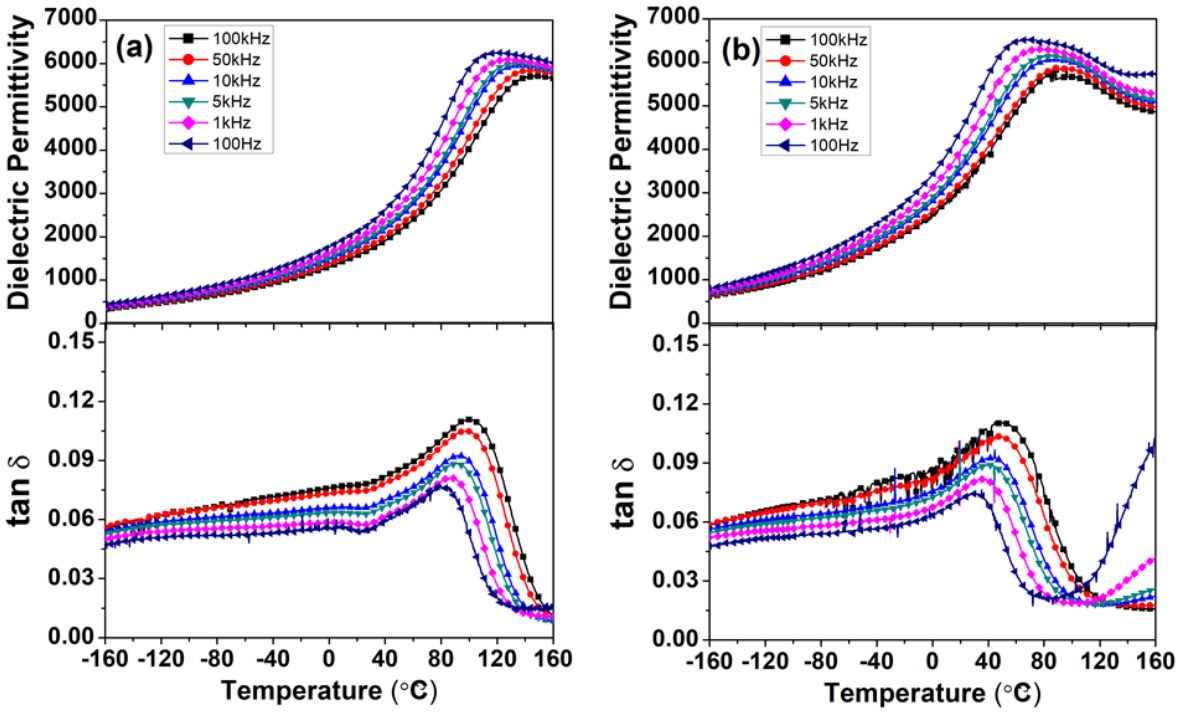

Figure 3. The temperature dependence of dielectric permittivity and loss for SBNLT-x: (a) x = 30 and (b) x = 38, highlighting the composition-induced influence on relaxor behaviour.

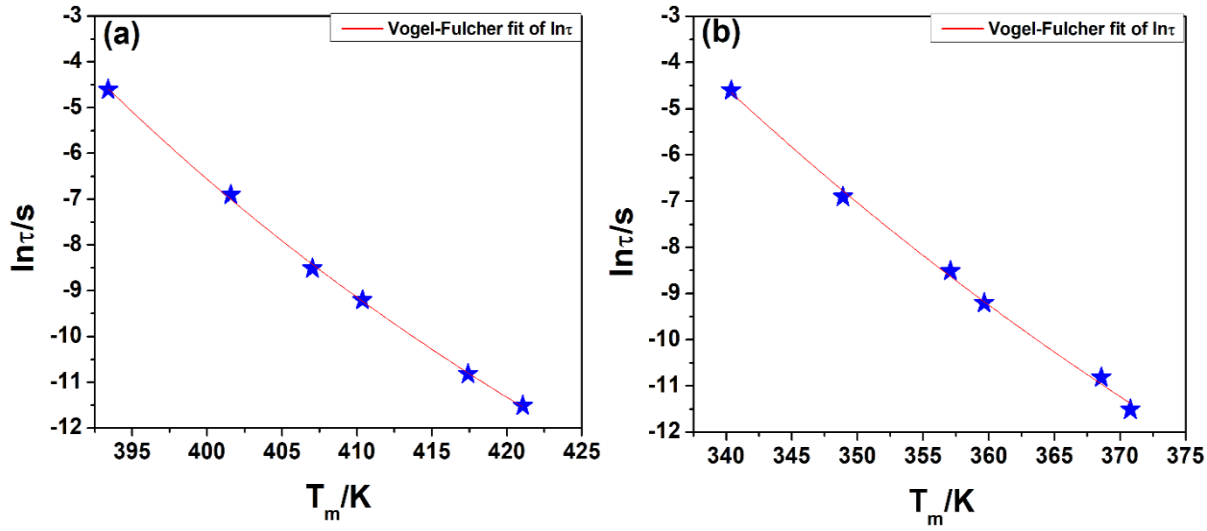

Figure 4. The natural logarithm of relaxation time ($\ln\tau$) as a function of temperature corresponding to the dielectric maxima (T_m) for SBNLT-x: (a) x = 30 and (b) x = 38 (The stars represent experimental data and the solid curves represent the fitting to the Vogel-Fulcher relation)

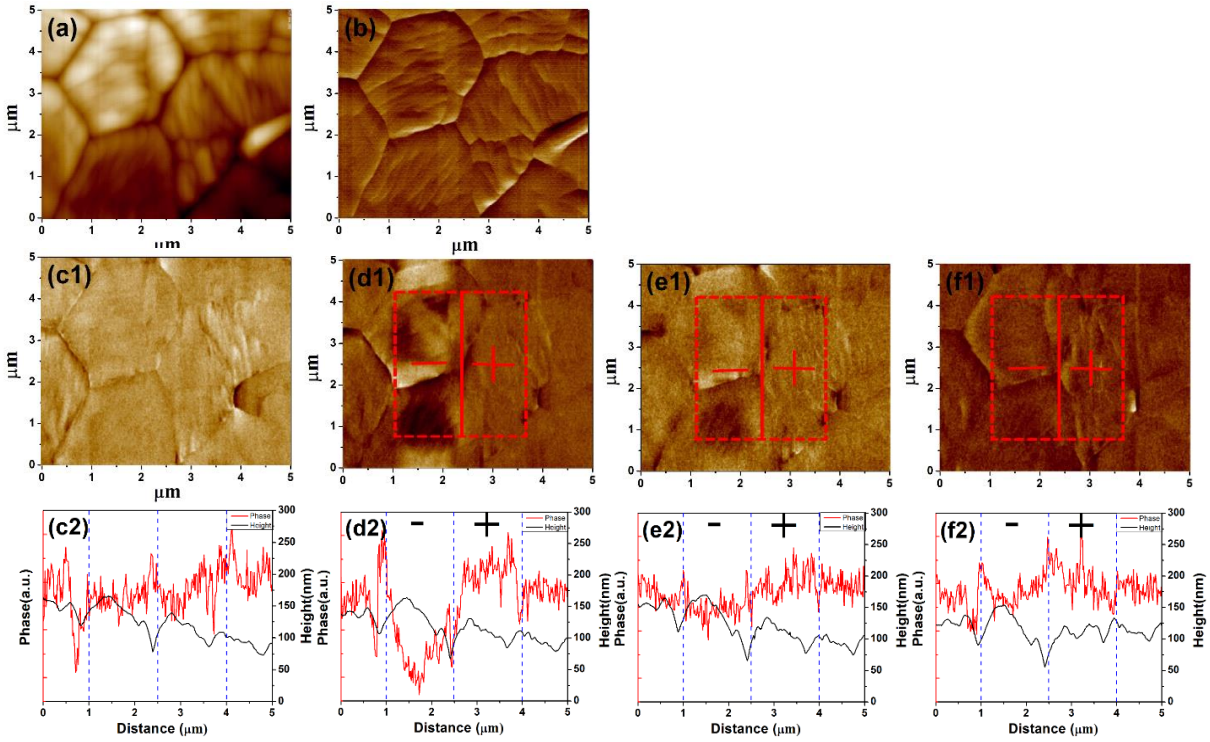

Figure 5. PFM images of an area of 5×5 µm^2 for SBNLT-30: (a) topography, (b) magnitude, (c1-f1) phase and (c2-f2) signal graphs. The phase and signal images acquired: (c1) (c2) before poling, (d1) (d2) right after poling, (e1) (e2) 15 minutes after poling and (f1) (f2) 30 minutes after poling. (Poling was conducted in the 3×3 µm^2 area in the centre, the red dashed lines in the phase image and blue dashed lines in the signal image correspond to the negative and positive poled areas, respectively.)

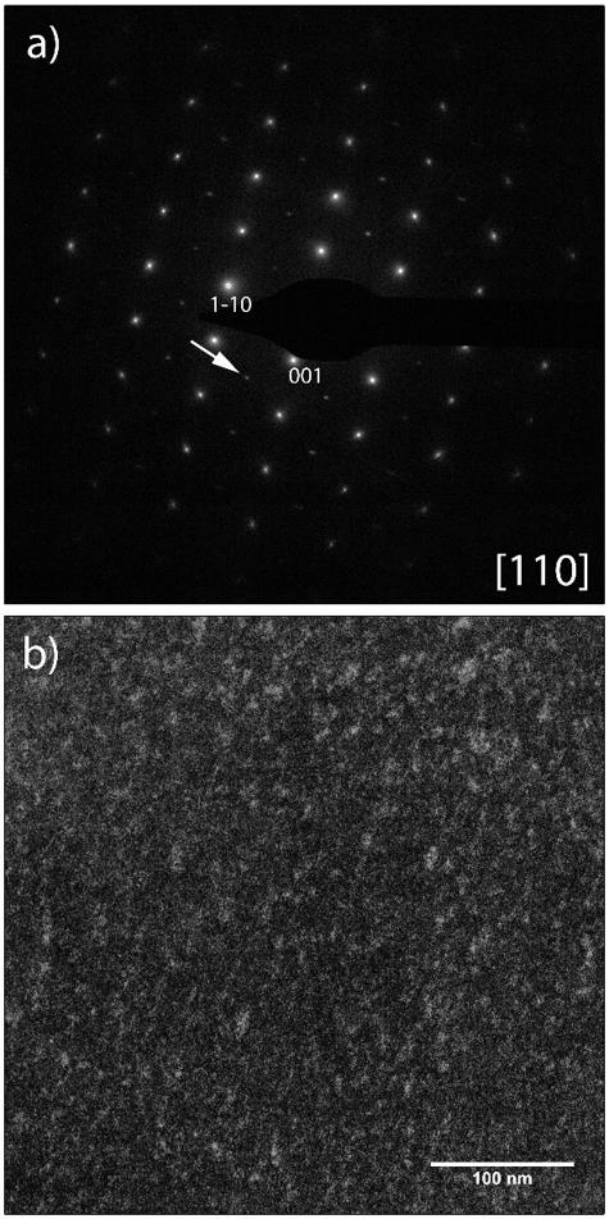

Figure 6. TEM analysis of SBNLT-30. (a) Selected area electron diffraction (SAED) pattern of the [110] zone axis. The pattern shows strong reflections of the cubic symmetry and weak superstructure reflections *1/2 (ooo)* (marked with arrow). (b) On axis dark field (DF) image. For imaging, a superstructure reflection has been used and thus the volumes with this ordering appear bright in the micrograph.

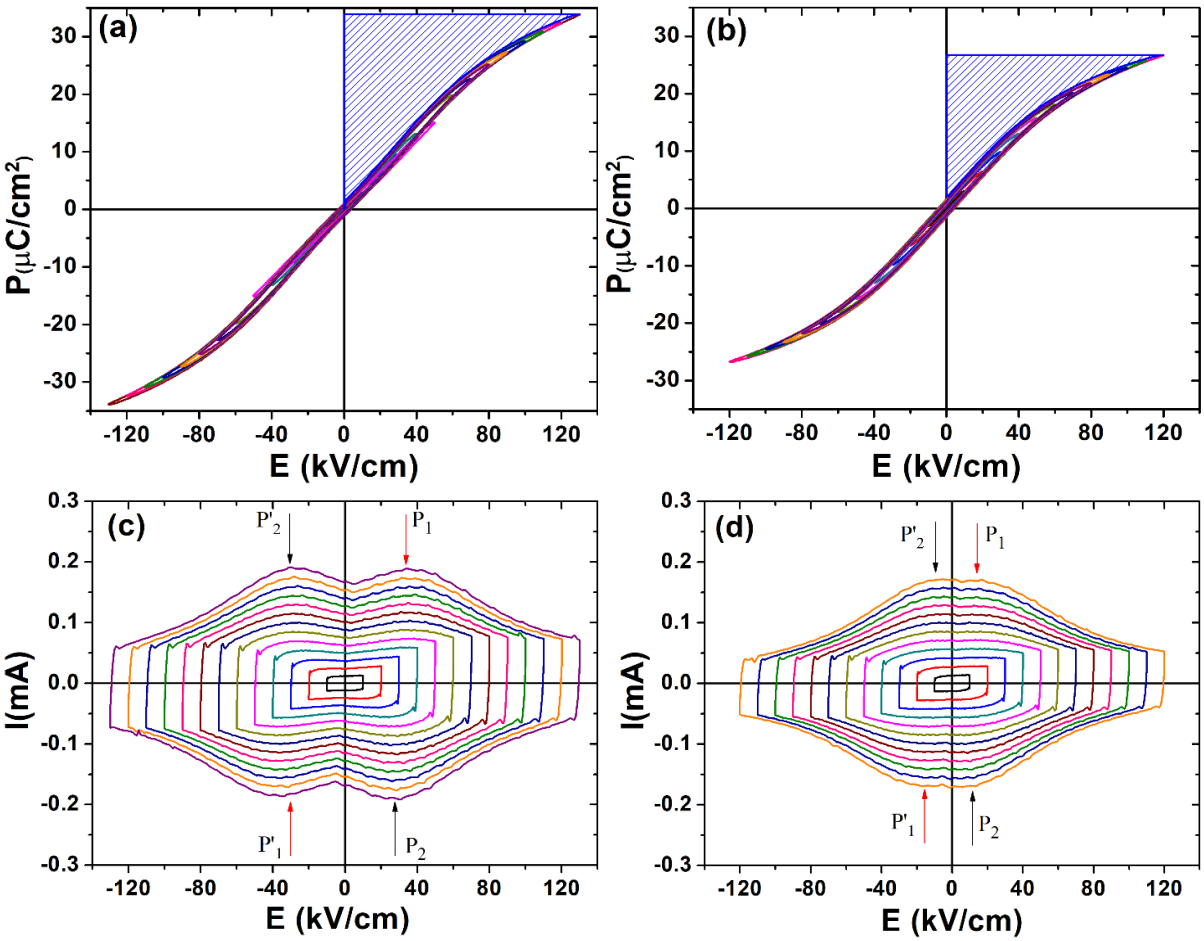

Figure 7. (a), (b) *P-E* and (c), (d) *I-E* loops of ceramic SBNLT-30 and SBNLT-38 at different electric field amplitudes (measured at room temperature and 10 Hz). Note that W_{rec} is represented by the blue hatched area in the *P-E* loops.

.

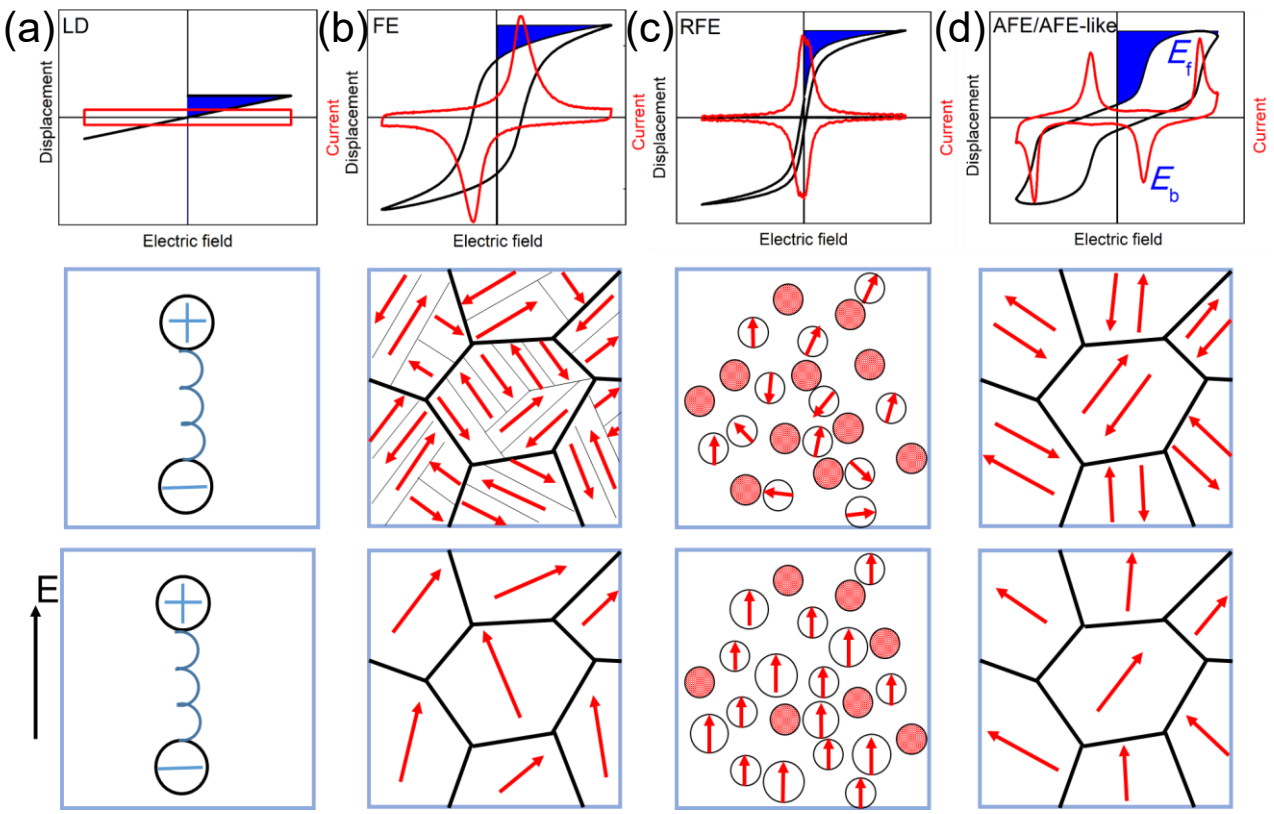

Figure 8. Schematic for the hysteresis loops and energy storage properties of (a) linear dielectrics (LD), (b) ferroelectrics (FE), (c) relaxor ferroelectrics (RFE) and (d) antiferroelectrics/antiferroelectrics-like (AFE/AFE-like). The blue printed area represents the recoverable energy density W_{rec}. The bottom panels illustrate the mechanism of dielectric behaviour for the four materials above. The red arrows in grains or domains mark the directions of polarization. In (a), the spring represents a dipole linked with field-independent dielectric permittivity. In (b), the dark and light black lines demonstrate the grain boundaries and ferroelectric domain walls, respectively. In (c), the PNRs are illustrated by the hollow circles. In (d) the dark lines represent the grain boundaries. Note that the forward field (E_f) and backward field (E_b) of the antiferroelectric-to-ferroelectric (AFE-FE) phase transitions are marked in (d).

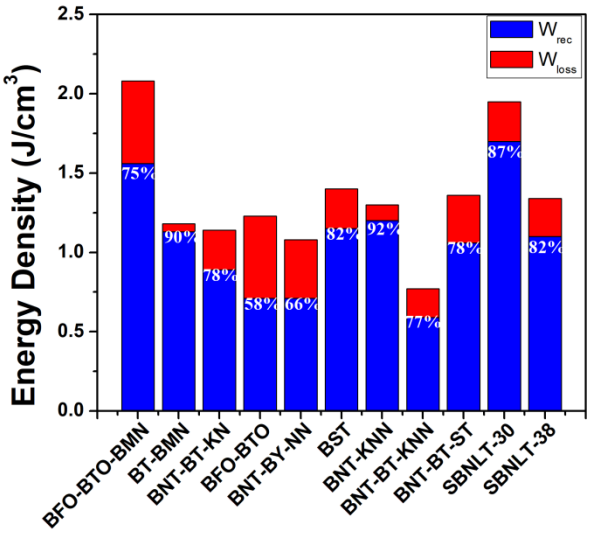

Figure 9. Assessment of the energy storage performance for lead-free ceramics systems. Note the high W_{rec} and η of our SBNLT-30 sample.[26, 50-57]